REVISED MANUSCRIPT

for publication in the

Journal of Power Sources

Investigations of the Structural Stability of Metal Hydride Composites by in-situ Neutron Imaging

Kai Herbrig[1,2], Carsten Pohlmann[1], Łukasz Gondek[3], Henryk Figiel[3], Nikolay Kardjilov[4], André Hilger[4], Ingo Manke[4], John Banhart[4,5], Bernd Kieback[1,2] and Lars Röntzsch[1,*]

[1]*Fraunhofer Institute for Manufacturing Technology and Advanced Materials IFAM, Branch Lab Dresden, Winterbergstraße 28, 01277 Dresden, Germany*

[2]*Technische Universität Dresden, Institute of Materials Science, Helmholtzstraße 7, 01069 Dresden, Germany*

[3]*AGH University of Science and Technology, Faculty of Physics and Applied Computer Science, al. A. Mickiewicza 30, 30-059 Krakow, Poland*

[4]*Helmholtz Center Berlin for Materials and Energy, Hahn-Meitner-Platz 1, 14109 Berlin, Germany*

[5]*Technical University Berlin, Department of Materials Science and Technology, Hardenbergstraße 36, 10623 Berlin, Germany*

*Corresponding author: phone: +49-351-2537-411; fax: +49-351-2537-399

e-mail: Lars.Roentzsch@ifam-dd.fraunhofer.de

Research Highlights

- In-situ imaging of metal hydride composites (MHC) with cold neutrons was performed.
- A swelling of 20-33 vol.-% of MHC upon hydrogenation was measured.
- MHC remain mechanically intact even if axial expansion is allowed.
- The heat transfer was improved by closing the gap between MHC and the container.
- Hydrogenation reaction fronts were directly observed.

Abstract

Metal hydride composites (MHC) with expanded natural graphite (ENG) exhibiting enhanced thermal conductivity and reduced porosity compared to metal hydride powders can enable a reversible, compact and safe way for hydrogen storage.

In this study, neutron imaging during cyclic hydrogenation was utilized to investigate the structural stability and the spatial-temporal hydrogen concentration of application-oriented MHC with 40 mm in diameter compared to a loose metal hydride powder. In particular, swelling and shrinking effects of a radially confined MHC which could freely expand upwards were studied. It was found that the loose powder bed was easily torn apart during dehydrogenation, which leads to increased thermal resistance within the hydride bed. In contrast, the thermal resistance between MHC and container wall was minimized since the initial gap closes during initial hydrogenation and does not reopen thereafter. Further cyclic hydrogenation caused MHC volume changes, i.e. an almost reversible swelling/shrinking (so-called “MHC breathing”). Moreover, neutron imaging allowed for the observation of reaction fronts within the MHC and the powder bed that are governed by the heat transfer.

Keywords

AB_2–type Ti-Mn alloy; metal hydride composite; heat and gas transfer; volume swelling; neutron radiography; neutron tomography

Graphical Abstract (for review)

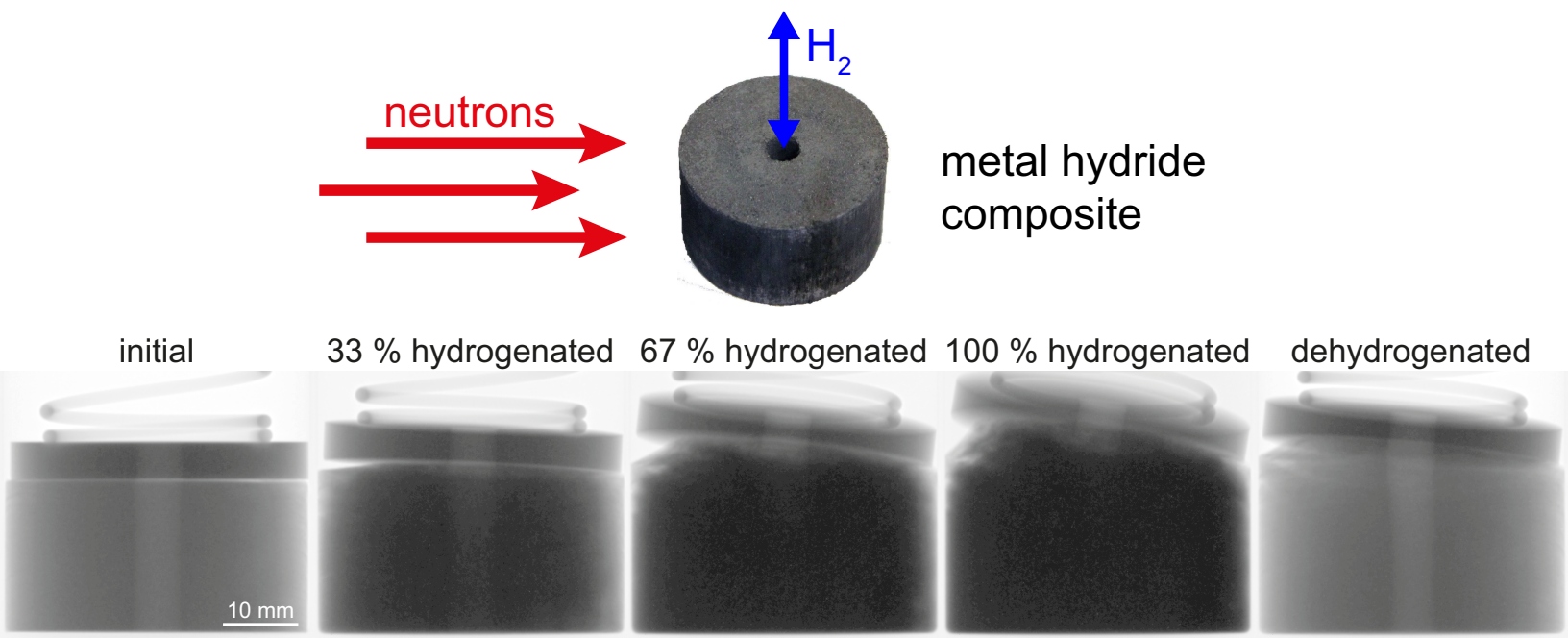

1 Introduction

Hydrogen offers a much higher heating value per mass[1] than conventional fuels. Therefore, hydrogen technologies might replace carbon-based fuel technologies in the future [1,2]. A hydrogen-based energy cycle could start with the production of hydrogen using a renewable energy source and end with its consumption at a later time at a different location, which is why hydrogen storage is important. Hydrogen gas at standard conditions has a very low mass density of about 89 mg/l. In order to reach useful volumetric capacities, different hydrogen storage technologies have been developed that rely on pressurization (up to 700 bar), on liquefaction at cryogenic temperatures (20 K), on adsorption in porous materials such as metal-organic frameworks (MOFs) or on chemical absorption, for example in hydrides [3]. Metal hydrides (MH) offer very high theoretical volumetric hydrogen storage densities[2] in the range of 100 g-H_2/l. MH are formed at low hydrogen gas pressures (several bars to a few tens of bars) and, for many transition metal (TM) alloys, MH are formed close to 'room temperature' (e.g. Fe-Ti-, Ti-Mn-, La-Ni-based hydrogen absorbing alloys) [4,6]. TM-based hydrogen absorbing alloys are advantageous whenever highest volumetric storage capacities are needed but low weight is not mandatory. Therefore, applications in the fields of backup power, materials handling (forklifts), marine or submarine are promising [7]. In this work, a commercially available AB_2-type Ti-Mn-based hydrogen-absorbing alloy called Hydralloy $C5_2$ was used, which absorbs hydrogen up to about 1.8 mass-% [8].

MH are often granules or powder. Because of the large volume content of porosity in powder beds (up to 70 vol.-%), the high volumetric storage capacity of MH vanishes. Moreover, the reduced thermal conductivity of MH powder beds lower the loading and unloading dynamics of respective storage tanks,

---

[1] Lower heating value of hydrogen: 33.3 kWh/kg; methane: 13.9 kWh/kg; gasoline: 12.4 kWh/kg [1].

[2] Metal hydrides ($Ti_{1.2}Mn_{1.8}H_{3.1}$): 100 g-H_2/l; liquid H_2 (20 K, 1 bar): 71 g-H_2/l; H_2 at 700 bar, 300 K: 39 g-H_2/l [4,5].

despite the often extremely fast intrinsic reaction kinetics of TM-based hydrogen absorbing alloys [9,10]. In order to improve the heat transfer and maintain high volumetric storage capacities graphite-containing metal hydride composites (MHC) are considered promising materials for solid-state hydrogen storage [11–15].

In this work, MHC based on Hydralloy $C5_2$ and expanded natural graphite (ENG) are investigated. During cyclic hydrogenation MHC are strongly influenced by crystal lattice expansion and contraction during hydrogenation and dehydrogenation, respectively [16]. In our previous work, we observed a high geometrical stability of MHC in combination with sufficient thermal conductivity and gas permeability throughout cyclic hydrogenation [15]. However, the MHC were cycled while being spatially confined by a strong metallic clamp that resisted the forces generated during hydrogenation and prevented macroscopic swelling of the MHC. This paper addresses swelling and shrinkage of MHC inside a cylindrical tank during cyclic hydrogenation and their non-destructive examination by in-situ by neutron imaging. In contrast to X-rays, hydrogen shows one of the highest attenuation coefficients for neutron radiation [17,18]. Hence, neutron imaging is very sensitive to the detection of hydrogen in materials [19–26]. Previously, we investigated a powdered $LaNi_5$-based hydride and the activation behavior of such MHC by high-resolution neutron imaging using small samples of 12 mm diameter [19,27]. In this work, the investigations focus on application-oriented MHC of 40 mm diameter in comparison to loose hydride powder beds. Both volume changes of the MHC and the spatial-temporal hydrogen concentration profile during cyclic hydrogenation are studied.

2 Experimental

2.1 Sample preparation

The AB_2-type hydrogen absorbing alloy Hydralloy $C5_2$ (51 mass-% Mn, 28 mass-% Ti, 14 mass-% V, 3 mass-% Fe, 3 mass-% Zr) purchased in form of granules from *GfE Metalle und Materialien GmbH* was milled for 5 min under argon using a rotation disk mill. Thereafter, MHC were fabricated as described in our previous work [15] by blending the Hydralloy powder with 5 mass-% expanded natural graphite (ENG). The mixture was then uniaxially compacted into cylindrical solid bodies (pellets) using a die of 39 mm diameter (cf. Figure 1 a). After applying a compaction pressure of 75 MPa a residual porosity of 32 vol.-% remained within the consolidated MHC (88 g total mass). For an equal axial hydrogen distribution, a central hole of 6 mm diameter was manufactured already during compaction by applying a core rod. One of the MHC samples was cut into halves vertically (cf. Figure 1 a). Moreover, a powdered sample was prepared by blending Hydralloy powder with alumina powder (Alcoa, 0.2-0.6 mm) in equal volume fractions (50:50 vol.-%). Alumina has a low attenuation coefficient for neutrons and does not react with hydrogen under the experimental conditions applied. Therefore, it is a suitable filler material to reduce the effective hydrogen concentration in the powdered sample for an improved imaging quality. All processing steps were performed in an inert atmosphere to avoid any surface passivation of the materials involved. The three different types of samples will be referred to as 'MHC', 'half-MHC' or 'hydride-alumina powder (HAP)' samples.

The samples were placed into aluminum alloy (AlMg3) containers (cf. Figure 1 a), which are almost "transparent" for neutrons. The temperature of the container wall was monitored by a thermocouple close to the sample. A moveable 5 mm or 10 mm thick steel plate was placed on top of the MHC samples. The position of the midpoint of the bottom side of the moveable steel plate was used to calculate the volume change of the MHC. For MHC samples, a spring with a modulus of 12 N/cm was

integrated into the sample container. This caused a mechanical pressure of at the most 0.03 MPa onto the MHC sample, which is negligibly small compared to the compaction pressure of 75 MPa and, thus, no further densification of the MHC is expected. Both the spring and the steel plate were added to keep the MHC at the bottom of the container during transportation and throughout all experiments (especially during rapid pressure releases) and to keep the MHC in shape in case loose parts or MHC fragments during cyclic hydrogenation occurred (cf. our previous work [27]). For the powdered sample, no spring was used. Instead, since loose powder is much more volatile than a compacted sample, the free volume above the powder was filled with glass fiber wool. This prevents powder material removal from the container to prefilter the gas during H_2 pressure release. In order to allow for a comparison between the results of the powder sample with the MHC no spring was integrated into the container when holding the half-MHC. To stabilize the half-MHC a thin aluminum plate was placed vertically in the middle of the container serving as a constraint of pellet expansion into the empty half. The samples within the containers were subjected to an activation procedure involving exposition to elevated temperatures (~125 °C) for at least 6 h under hydrogen (99.9999 % purity) with varying pressures up to 8 bar. After activation, the MHC samples readily absorb hydrogen. The HAP sample was additionally hydrogenated and dehydrogenated 5 times at room temperature, a state called ‘as-cycled’ in the following.

2.2 Cold-neutron imaging

The neutron imaging experiments were conducted at the beamline CONRAD (V7) of the research reactor BERII at the Helmholtz Center Berlin for Materials and Energy in Berlin, Germany (HZB) [27–31]. A 200-µm thick ^{6}LiF scintillating screen with a side length of about 20 cm was selected for the conversion of neutrons into visible light. A pixel resolution of 69 µm was achieved, i.e. one pixel represents an area of (69×69) µm^2. The sample was mounted close to the front side of the scintillator

on a goniometric table allowing for rotation, translation and tilting. The optical path from the scintillator to the focusing optical system and CCD camera is folded by a mirror to avoid any radiation damage of sensitive components by the neutron beam. The Andor DW436N-BV CCD camera with 2048×2048 pixels was cooled by Peltier elements to −50°C in order to keep spurious signals at lowest levels. The exposure time used for the experiments was 30 s for every projection image in the neutron radiography experiments. Note that after each exposure readout took about 7 s. Thus, 37 s elapse between the beginnings of two subsequent images. The outer walls of the container were charged with pressurized air at room temperature to improve the heat transfer between the container and the ambience.

2.3 Hydrogenation set-up

The gas supply during hydrogenation/dehydrogenation cycles was controlled manually. In order to ensure fast hydrogenation, a fast H_2 pressure step from 1 bar to 30 bar was achieved by a pressure reducer with predefined final pressure and quickly opening the valve connecting it to the hydride vessel. Alternatively, a slow pressure build-up to 30 bar for a controlled and homogeneous hydrogenation was realized using a mass flow controller with a constant inflow rate of 100 ml/min (STP). For dehydrogenation, the H_2 pressure inside the container was decreased to 1 bar with a constant hydrogen outflow of 100 l/h (STP) using a manually controlled float flow regulator. Hydrogen with a purity of 99.999 % and deuterium with a purity of 99.8 % were used for the experiments at the beamline. Please, note that the main impurity in the deuterium gas is hydrogen deuteride (HD).

2.4 Imaging procedure and analysis

According to Beer-Lambert's attenuation law the intensity I of the transmitted neutron beam can be obtained according to equation (1), with I_0 as the intensity of the incident neutrons, Σ as the attenuation coefficient and d as the path length. It must be noted that the obtained information is integrated along the path of the neutrons within the sample. Image normalization (I / I_0) was performed as described in our previous work [19,27].

$$I = I_0 e^{-\Sigma d} \tag{1}$$

The absorbance A can be calculated in accordance with equation (2). Considering equation (1) and (2), the absorbance A gives Σd, resp. $\Sigma' \rho d$ with $\Sigma' = (\Sigma/\rho)$ as the mass attenuation coefficient, which only depends on the nuclei and neutron wavelength. The area integral of the absorbance within an image results in $m\Sigma'$, with m the mass of the corresponding material within the volume of interest (VOI) in the sample. For a known Σ' the mass of the corresponding material can be calculated. However, the effective Σ' for hydrogen is not constant because of scattering and beam hardening effects which are caused by the large amount of hydrogen within the sample. In the following, the area integral of the absorbance is used as a semi-quantitative signal of the hydrogen content within the sample. In this case, the whole internal volume of the container including the steel plate and the spring is chosen as VOI.

$$A = -\ln \frac{I}{I_0} \tag{2}$$

For neutron tomography of the dehydrogenated MHC, two radiographic images (30 s exposure time) and for tomography of the deuterated MHC three radiographic images for each of the 500 angles of

rotation distributed over 360° were acquired. Each set of images per angle step was processed by a median filter to obtain images with better signal to noise ratio. These 500 images were used for reconstruction of the three-dimensional (3D) distribution of the attenuation coefficient. A beam hardening correction method with a polynomial approach was applied [32].

2.5 Reconstruction of the local attenuation coefficient from radiography of axisymmetric samples

As mentioned before, the signal at the detector (absorbance A) is the integral value of the attenuation along the path of the neutron ray through the sample. Since the sample and the container can be seen as axisymmetric, it is reasonable to assume, that the projection image at the detector originates from an axisymmetric distribution of the attenuation coefficient. Then, the spatially varying attenuation coefficient of the axisymmetric sample can be reconstructed by applying an algebraic reconstruction algorithm, which is illustrated in Figure 1 b using only a single radiographic image. This allows for a tomography-like reconstruction of a vertical slice of the sample during cyclic hydrogenation [33].

First, the sample is discretized pixelwise into $M \times N$ adjacent rings with a quadratic cross-section. An constant attenuation coefficient $\Sigma_{m,n}$, ($1 \leq m \leq M$, $1 \leq n \leq N$), is assigned to every ring. Furthermore, the neutron beam is also discretized pixelwise into $M \times K$ quadrants ($1 \leq k \leq K$, $1 \leq m \leq M$, $K = N$). A pixel represents one discrete neutron ray. The contribution of the n^{th} ring to the attenuation of the k^{th} neutron ray is then given by the geometric distance $C_{k,n}$ the ray travels through this ring, c.f. Eq. (3), multiplied by the attenuation coefficient of that ring. These attenuations are summed up to the total attenuation of the k^{th} ray according to Eq. (4).

$$C_{k,n} = 2 \cdot \begin{cases} \sqrt{r_n^2 - r_{k-1}^2} - \sqrt{r_{n-1}^2 - r_{k-1}^2} & , \quad n \geq k \\ 0 & , \quad n < k \end{cases} \tag{3}$$

with $1 \leq k \leq N$, $1 \leq n \leq N$, $r_0 = 0$

$$A_{k,m} = \sum_{n=1}^{N} \Sigma_{m,n} C_{k,n} \tag{4}$$

$C_{n,k}$ is a triangular matrix, which facilitates numerical treatment. To derive the attenuation coefficients $\Sigma_{m,n}$ the linear system (4) was solved separately for each m^{th} slice.

Prior to reconstruction, the symmetry line on the image was determined slice-wise and fitted to a straight line separating the image into two halves, which were treated independently. In the following, the reconstruction of one half is presented. The symmetry line determination and the reconstruction algorithm was implemented in MATLAB.

3 Results and discussion

3.1 Structural investigation of Metal Hydride Composites (MHC) and of loose hydride powders during cyclic hydrogenation by in-situ radiographic imaging and tomography

3.1.1 Loose Powder Bed

Three radiographic images are depicted in Figure 2 a-c showing different states during cyclic hydrogenation of a powdery sample containing 50 vol.-% alumina (HAP). Starting from the as-cycled state (cf. Figure 2 a) the powder was hydrogenated (cf. Figure 2 b). The powdery reaction bed was slightly compacted because of the fast pressure build-up during hydrogenation, superimposing the

particle expansion due to hydrogenation. During fast dehydrogenation (cf. Figure 2 c), the powder bed was torn apart as the pressurized hydrogen between the powder particles and the absorbed hydrogen within the particles vacates upon depressurization. This partially lifts the loose powder and open gaps within appear. Such gaps hinder thermal flow and lower the effective thermal conductivity inside the sample. Even in the fully dehydrogenated state where no further dehydrogenation and, therefore, gas flow occurs, the gap remains. Due to the low pourability of the irregularly shaped powder particles an arching effect occurs which is well-known in granular materials science [34]. This effect stabilizes the lifted powder bed against reconsolidation. With the next pressure build-up during the following hydrogenation cycle the lifted powder was then pushed back down (not shown, but similar to Figure 2 b). From the viewpoint of an engineering system, fast hydrogen un-/loading has several implications: Loose hydride powder beds can be very volatile and powder particles as well as agglomerates can be easily lifted and then settle again at a different site. Thus, a tank system has to be carefully protected against powder particle displacement, since it may lead to the damage of valves or other parts. Moreover, because of the decrepitation of metal hydride particles it is necessary to install a particle filter for much smaller particle sizes compared to the as-milled state [35]. Especially in high-pressure hybrid hydrogen storage tanks [36] – a combination of pressurized hydrogen systems (350 bar/700 bar) with metal hydride fillings – even very small particles can be extremely harmful for valves and connectors. Furthermore, a lowered thermal conductivity caused by any gaps between particles or the hydride particle bed and the container walls (cf. section 3.2) will slow down the hydrogen sorption dynamics. A continuous movement of powder particles may lead to a progressive densification (tapped density) of some parts of the powder bed, since fine powder created by decrepitation usually accumulates at the bottom [37]. Densified powder regions will cause the development of increased mechanical stresses during hydrogenation (local volume swelling), which negatively impacts the structural integrity of the

tank [38]. From this perspective, a compacted hydride powder with limited free particle movement is advantageous.

3.1.2 Compacted Composite

The first hydrogenation cycle of a MHC starting from the as-activated state is shown in Figure 2 d-h. Here, the first hydrogenation cycle was carried out slowly to obtain a better temporal resolution of the structural changes. In the following a fast dehydrogenation similar to the one of the loose powder bed was performed. The as-activated state (cf. Figure 1 a and Figure 2 d) shows a homogeneous MHC with the moveable steel plate on top that is connected with the container lid by a spring. The screws for tightening the container lid, which are located outside the container, are also visible in the background (cf. Figure 1 a). The central hole inside the MHC can also be seen clearly. During hydrogenation (cf. Figure 2 e-g) the MHC absorbs hydrogen, which strongly attenuates the neutron beam. Thus, the MHC appears continuously darker in each projection image. At the end of the hydrogenation the central hole is only barely visible anymore. During hydrogenation the MHC continuously increases in height, which is correlated to the crystal lattice expansion of the hydrogen-absorbing alloy with increasing hydrogen content. Based on neutron diffraction data the crystal lattice volume expansion during hydrogenation (with deuterium) of $Ti_{1.2}Mn_{1.8}$ ($Ti_{1.2}Mn_{1.8}D_{3.1}$) is 26.5 % [4]. Since the hydride under investigation is an AB_2-type Ti-Mn alloy, it is reasonable to assume that the crystal lattice expansion of this hydride is similar to that of $Ti_{1.2}Mn_{1.8}$. In this case, the crystal lattice expansion of the hydride forming alloy might have been fully compensated by reducing the internal porosity of the MHC without any macroscopic volume change of the MHC. However, this would involve a free relative movement of the phases inside the MHC during the hydrogenation-induced swelling. However, the hydrogen absorbing alloy under investigation is a hard and brittle intermetallic compound and the corresponding particles have irregular

shapes. Hence, only a very limited particle movement and/or reorientation is possible. Consequently, the hydride forming particles do not freely fill the porosity and, therefore, a macroscopic volume change of the MHC occurs. In particular, if the MHC can freely expand upwards, the crystal lattice expansion of the hydride forming alloy causes a significant macroscopic swelling of the whole MHC in the upward direction, too. This swelling of the MHC is obviously not fully homogeneous as the steel plate slightly tilts. The cylindrical MHC expands preferably axially at its center while the regions of the MHC close to the tank wall show a less pronounced expansion. This is most likely related to friction between the MHC and the tank wall, which causes additional stress to the container even if the MHC can expand axially. This is of utmost importance regarding the construction and design of hydrogen storage containers based on MHC [39]. After dehydrogenation (cf. Figure 2 h), the central hole is visible again. However, the evolved shape of the MHC partly remains. Hence, if a MHC, which is allowed to expand freely in at least on direction, is exposed to cyclic hydrogenation involving macroscopic swelling, this volume changes are not fully compensated by the internal porosity of the MHC.

Radial swelling was also observed. Figure 3 clearly shows that the initial small gap (~500 µm, allowing inserting the MHC) between the MHC and the container wall closes during hydrogenation. Thus, an improved heat transfer between the MHC and the wall of the container can be presumed. This gap does not reopen during dehydrogenation (cf. Figure 3 c). Therefore, the improvement is permanent.

As mentioned before, hydrogenation during the first cycle was performed slowly with a resulting hydrogen uptake rate of about 0.01 mass-%/min. At the end of the first cycle the MHC had absorbed 1.4 mass-% hydrogen. The MHC was then cycled three more times until another slow hydrogenation was performed. During subsequent slow hydrogenation cycles (i.e. in the 5th cycle) the examined pressure-concentration developments refer to a typical behavior known from pressure-concentration isotherms which were measured in our previous work [40]. In this case, the hydrogen feeding rate is low enough to follow the materials equilibrium pressure. In this cycle, a reversible hydrogen capacity of

1.35 mass-% was observed. For comparison, in our previous work on similar MHC [15], a comparable reversible hydrogen capacity of 1.45 mass-% at 20 °C was achieved. In the 6th cycle, the MHC was loaded with deuterium. This implies that during this cycle the remaining hydrogen after the 5th cycle was replaced by deuterium (rinse cycle). For the purpose of tomography of a loaded MHC, the MHC was then slowly charged with deuterium in the 7th cycle. Deuterium was used because the attenuation of a hydrogenated MHC is too strong to perform a tomography (cf. Figure 2 g). The associated pressure-concentration development referred to a distinctly lower plateau pressure (3 to 5 bar lower) than with hydrogen as observed in the 5th cycle. This isotope effect is also known for other hydrides [41]. If deuterium is used instead of hydrogen to reduce the attenuation of neutrons in order to investigate larger MHC-based tanks the different thermodynamics have to be considered, since the equilibrium pressure greatly influences the dynamics of a hydride-based tank system.

As mentioned above volume swelling and shrinkage of the MHC occurred during cyclic hydrogenation (cf. Figure 2 d-h). In Figure 4, this volume swelling of the MHC throughout cyclic hydrogenation with respect to the initial volume (V_0) in the as-activated state is depicted. During the first hydrogenation the MHC volume increases continuously to about 1.3 V_0. During dehydrogenation this swelling is then reversibly reduced to 1.2 V_0. For the following hydrogenation cycles a similar behavior was observed: During hydrogenation the MHC expanded again to about 1.31 V_0 to 1.33 V_0, after which an irreversible swelling of 1.23 V_0 to 1.24 V_0 remained in the dehydrogenated state. The largest swelling occurred within the first hydrogenation cycle (1.3 V_0), after which only minor increases took place (1.31 V_0 to 1.33 V_0). In this regard, an almost reversible volume change between the hydrogenated (≈ 1.3 V_0) and the dehydrogenated state (≈ 1.2 V_0) was observed. This is denoted as MHC “breathing” in the following.

In Figure 5, volume rendered images (a-d) as well as vertical (e-h) and horizontal (i-l) slices are presented based on the tomographic reconstruction of the MHC at four different stages throughout cyclic hydrogenation: As-activated (a, e, i), dehydrogenated after the 1st (b, f, j) and the 5th cycle (c, g, k)

as well as deuterated in the 7th cycle (d, h, l). The vertical slices clearly show the MHC with its central hole and the steel plate on top with the spring above. The vertical and the horizontal slices of the as-activated state (e, i) exhibit no damage of the MHC due to transportation or fabrication. The MHC appears homogeneous and exhibits no cracks or defects. The vertical slices (f-h) after the 1st and 5th hydrogenation cycle in the dehydrogenated state and within the 7th hydrogenation cycle in the deuterated state reveal an alteration of the MHC's shape compared to the as-activated state. The MHC is confined at the bottom and radially but it can freely expand upwards. At the top, where free space for expansion is available, cracking occurred while the bottom part remains crack-free. A crack starting from outside at the top of the MHC proceeds diagonally downwards. Smaller MHC with a diameter of 12 mm investigated previously [27] also cracked preferably at the top but the cracks were aligned horizontally. Also many small cracks were observed, whereas in this work few larger cracks occur, which are more diagonally aligned. This obvious difference might have been caused by differences in the ratio between the MHC diameter and that of the central hole (12:4 instead of 40:6) and/or differences in the surface-to-volume ratio which influences the friction between the MHC and the container wall during expansion. Moreover, the central hole meant to promote free hydrogen distribution shrinks continuously. Again, at the top the shrinkage of the hole is less pronounced than close to the bottom of the MHC where the inhibited vertical expansion causes radial swelling, thereby narrowing the central hole. However, the highest degree of shrinkage is not located directly at the bottom of the MHC, indicating that friction between the MHC and the lower tank wall plays an important role in the expansion behavior. Indeed, mechanical stabilization of the central hole, for example by a sintered porous tube, would be advantageous for engineering systems.

The horizontal slices (cf. Figure 5 i-l) clearly show a decreasing attenuation of the MHC throughout cyclic hydrogenation. Because of the swelling of the MHC its mass density decreases, however, not homogeneously. In Figure 6, the mean attenuation in axial direction within a specified volume of interest

(VOI, cf. Figure 5 e, i) is presented. Under the assumption that the linear attenuations of the hydrogen-absorbing alloy and graphite are constant within the MHC, a change in the mean attenuation directly refers to an altered density and translates into a changed porosity and, hence, different extents of swelling/shrinkage. Within the as-activated MHC the mean attenuation is quite constant, representing a homogenous MHC inside. During cyclic hydrogenation the mean attenuation notably changes in axial direction. At the top of the MHC a distinct lower mean attenuation than at the bottom is observed. Thus, at the bottom the increase in porosity (macroscopic swelling) is less pronounced than at the top. As a consequence, the largest expansion and shrinkage also occurs at the top of the MHC. The discontinuity in the curve of the mean attenuation coefficient at the top of the deuterated MHC refers to a crack, which is clearly visible in Figure 5 h.

3.2 In-situ radiographic imaging of MHC and hydride powder during hydrogenation

In the previous section, radiographic imaging during hydrogenation and tomography of certain states of the MHC were used to investigate the structural changes of a MHC and a loose hydride powder bed. In this section, the spatial-temporal hydrogen distribution during hydrogenation and dehydrogenation of a MHC compared to a hydride powder bed is addressed. Because a fully hydrogenated 40 mm MHC technically stops the neutron beam (cf. Figure 2 g) no evaluation in this regard was possible. Therefore, the hydrogen concentration along the pathway of the neutron beam (radial plane of the MHC) was halved using a half-MHC, thus increasing neutron transmission. Compared to a full MHC, heat transport within the half-sample remains almost unchanged because its cutting plane is a symmetry plane with no heat flux perpendicular to it but the mass transport of hydrogen will be enhanced due to the shorter pathways through the cutting plane. However, in our previous work it has been demonstrated that the

transport of hydrogen in such MHC as well as the intrinsic kinetics of the hydride are not the rate-determining step and that heat transfer determines the system kinetics [27,40].

To ensure that the half-MHC and the loose powder sample that occupies the entire volume are comparable, the hydride powder was mixed with 50 vol.-% alumina (HAP sample). In this regard the performance of the HAP sample is enhanced compared to a pure hydride powder mixture because of the reduced effective heat source density with alumina that damps the temperature increase.

In Figure 7, the temperature, the hydrogen gas pressure and the integral absorbance during hydrogenation and dehydrogenation of the half-MHC and the HAP are shown. The integral absorbance (cf. equation (2)) is related to the hydrogen content within the container, including the hydrogen in the actual half-MHC and the compressed gas within the free volume and in the internal porosity of the half-MHC. The amount of hydrogen within the half-MHC is still high and due to scattering and beam hardening effects any conversion of the attenuation into hydrogen concentration is not reliable. The area integral of the absorbance is not strictly linear with the amount of hydrogen. Yet, an increase of the integral value is related to an increased total hydrogen content. As the hydrogen pressure rises almost instantaneously up to 30 bar for both samples hydrogenation occurs immediately. The hydrogen content (area integral of absorbance) increases steeply. For the half-MHC, 97 % of the final value of the area integral is achieved within 3 min while for the HAP 4.5 min are needed. Note that the effective heat source density for HAP is reduced by 50 %, which increases the loading rate compared to a loose powder sample significantly. Still, the time needed for loading the half-MHC is much shorter compared to the HAP. The temperature increases because of the exothermic hydrogenation reaction and decreases as the hydrogenation rate decreases (cooling down to ambient temperature). The temperature peak (temperature of the container wall) for the half-MHC is higher than for the HAP because of the slower heat transfer and the lower hydrogen content of the HAP. For dehydrogenation the similar behavior is observed.

In Figure 8, reconstructions of the radial attenuation coefficient based on single radiographic images (see section 2.5) throughout hydrogenation and dehydrogenation of the half-MHC and the HAP sample are shown. Here, the right half of the reconstruction is shown. Both samples were cycled five times prior to this experiment.

In Figure 8, images a1 and b1 represent the starting condition (as-cycled, dehydrogenated). Images a2, b2 and a3, b3 show the radial attenuation coefficients of the samples during hydrogenation, images a4 and b4 represent the fully hydrogenated state and the following images a5 to a7 and b5 to b7 illustrate the samples during dehydrogenation. A higher radial attenuation coefficient can be attributed to a higher local hydrogen concentration and vice versa. In Figure 8, image a4 shows the hydrogenated state of the half-MHC. Compared to the MHC the hydrogen content of the half-MHC was reduced. Yet, the hydrogen content is still high enough, so that the image is affected by beam hardening and scattering effects. This leads to the spurious effect that hydrogen contained in the outside regions of the half-MHC "shields" the neutron beam (i.e. mainly the neutrons with the lowest energies) from the inside and scattered neutrons additionally reduce the contrast. This can be seen, for example, for the concentric hole in the center of the half-MHC which almost disappears in the hydrogenated state while it is clearly visible in the dehydrogenated state. Furthermore, the reconstructed attenuation coefficient inside the hydrogenated half-MHC appears lower than outside. In Figure 8 a, at the radial interface between the half-MHC and the sample container the attenuation coefficient is apparently higher than within the residual half-MHC volume. This is a reconstruction artifact due to a slight rotational misalignment of the half-MHC. The cutting plane of the half-MHC is not perfectly perpendicular to the neutron beam. Thus, the reconstruction yields in an artificial attenuation at the outer rings (cf. Figure 1 b) of the discretized half-MHC. Yet, in this case a semi-quantitative evaluation of the hydrogen concentration is possible and the hydrogenation and dehydrogenation reaction fronts within both samples can be clearly tracked.

Within both samples, hydrogenation starts preferably at the thermalized container walls where the heat of reaction can dissipate fastest. Within the half-MHC, a distinct reaction front starting radially from the container walls and axially from the bottom and from the top are observed. Hydrogenation of the HAP proceeds smoother than of the half-MHC. The HAP sample has a lower heat source density because of the mixture with non-reactive alumina. This damps the temperature increase and equalizes the local hydrogenation rate within the HAP. Because of the lower overall hydrogen content of the HAP sample scattering and beam hardening in the hydrogenated state is less pronounced compared to the half-MHC sample. The dehydrogenation also starts from the outside of the samples close to the thermalized container walls. MHC show an anisotropic thermal conductivity [14,15]. A much higher thermal conductivity is achieved radially than axially. During (de-)hydrogenation of the half-MHC, axial heat transfer clearly has a much lower impact than radial heat transfer as the radial reaction front proceeds much faster than the axial front. However, for cylindrical hydrogen storage systems with a small length-to-diameter ratio axial heat transfer has to be considered. As already mentioned in section 3.1, the HAP sample was torn apart during dehydrogenation and developed additional gaps within the powder bed. The attenuation coefficient and the hydrogen content is much higher at the gap. Thus, in addition to the low thermal conductivity of loose powder beds, these gaps further inhibit heat transfer and slow down the system kinetics.

Tearing did not start during the fastest pressure release but after the hydrogen pressure had already dropped from 30 bar to 8.6 bar/5.7 bar (cf. Figure 7 b between 10.5 min and 11 min; also see video 3, online video data). The equilibrium pressure for dehydrogenation of this particular hydride at 23 °C is between 8 bar and 6 bar [40]. In this sense, the release of hydrogen from the hydride itself could have caused tearing of the HAP. In our previous work, where we investigated a powder reactor bed based on $LaNi_{4.8}Al_{0.2}$, a similar observation was made: During desorption the powder was torn apart as the pressure reached the equilibrium pressure level. This might be a general rule for powder samples. The

effect might be triggered by the shrinkage of the hydrogenated particles during dehydrogenation, causing reduced interlocking between the particles and, hence, lowered interparticle cohesion.

4 Conclusions

Graphite-containing metal hydride composites (MHC) are suitable for solid-state hydrogen storage due to their enhanced thermal conductivity, high volumetric hydrogen capacity and better structural stability compared to loose hydride powders. MHC and a hydride powder bed (HAP) were investigated by in-situ neutron radiography and tomography during cyclic hydrogenation. Within the container, the samples were confined in the radial direction and at the bottom, but could freely expand upwards. The main results can be summarized as follows:

- Due to the high sensitivity of neutron imaging towards hydrogen the hydrogenation and dehydrogenation of MHC and HAP could be directly observed.
- Swelling of the MHC during cyclic hydrogenation occurred because of the crystal lattice expansion during hydrogenation of the hydrogen-absorbing alloy within the MHC. The MHC expanded to about 131-133 % of its initial volume in the hydrogenated state and an irreversible swelling of about 123-124 % remained in the dehydrogenated state. Cyclic hydrogenation caused an almost reversible swelling/shrinking (so-called “MHC breathing”).
- The mass density within a MHC developed inhomogeneously along the axis. The largest swelling and shrinkage occurred at the top of the MHC (open end). Friction between the MHC and the container walls were identified to influence the expansion behavior, which in turn causes additional mechanical stress on the container.

- MHC in the as-activated state are uniform in density and exhibit no visible cracks or defects. During cyclic hydrogenation, cracking occurred at the top while the bottom appeared to remain free of cracks. Overall, MHC remained mechanically intact during cyclic hydrogenation even if free axial expansion in one direction was allowed.
- The initial gap (~500 µm) between the MHC and the container wall closes during hydrogenation due to swelling of the hydride and remains closed during dehydrogenation. Hence, the improved heat transfer into the container wall is preserved.
- During instantaneous dehydrogenation the HAP was torn apart, causing a pronounced powder movement within the sample container. MHC showed little particle movement.
- During hydrogenation / dehydrogenation, reaction fronts within the MHC and the HAP were observed, which were ruled by heat transfer characteristics.

5 Acknowledgement

This work was partly funded by the Friedrich-und-Elisabeth-Boysen-Stiftung and by the BMBF (Federal Ministry of Education and Research of Germany; contract no. 03EK3020A), all of which is gratefully acknowledged. Also, the authors wish to thank Fabian Multrus for implementing the reconstruction algorithm in MATLAB®.

References

[1] L. Schlapbach, A. Züttel, Nat. 414 (2001) 353–358.

[2] K. Mazloomi, C. Gomes, Renew. Sustain. Energy Rev. 16 (2012) 3024–3033.

[3] A.F. Dalebrook, W. Gan, M. Grasemann, S. Moret, G. Laurenczy, Chem. Commun. 49 (2013) 8735–8751.

[4] D. Fruchart, J.L. Soubeyroux, R. Hempelmann, J. Less Common Met. 99 (1984) 307–319.

[5] J.W. Leachman, R.T. Jacobsen, S.G. Penoncello, E.W. Lemmon, J. Phys. Chem. Ref. Data 38 (2009) 721–748.

[6] B. Sakintuna, F. Lamari-Darkrim, M. Hirscher, Int. J. Hydrog. Energy 32 (2007) 1121–1140.

[7] U. Eberle, M. Felderhoff, F. Schüth, Angew. Chem. Int. Ed. 48 (2009) 6608–6630.

[8] GfE Metalle und Materialien GmbH, Hydralloy C inspection certificate, 2011.

[9] V. Skripnyuk, M. Ron, J. Alloy Compd. 293-295 (1999) 385–390.

[10] S.S. Murthy, J. Heat Transf. 134 (2012) 031020.

[11] K.J. Kim, B. Montoya, A. Razani, K.-H. Lee, Int. J. Hydrog. Energy 26 (2001) 609–613.

[12] H.-P. Klein, M. Groll, Int. J. Hydrog. Energy 29 (2004) 1503–1511.

[13] A. Chaise, P. de Rango, P. Marty, D. Fruchart, S. Miraglia, R. Olivès, S. Garrier, Int. J. Hydrog. Energy 34 (2009) 8589–8596.

[14] C. Pohlmann, L. Röntzsch, S. Kalinichenka, T. Hutsch, B. Kieback, Int. J. Hydrog. Energy 35 (2010) 12829–12836.

[15] C. Pohlmann, L. Röntzsch, F. Heubner, T. Weißgärber, B. Kieback, J. Power Sources 231 (2013) 97–105.

[16] B. Charlas, A. Chaise, O. Gillia, P. Doremus, D. Imbault, J. Alloy Compd. 580 (2013) 149–152.

[17] V.F. Sears, Neutron News 3 (1992) 26–37.

[18] M. Strobl, I. Manke, N. Kardjilov, A. Hilger, M. Dawson, J. Banhart, J. Phys. D 42 (2009) 243001.

[19] Ł. Gondek, N.B. Selvaraj, J. Czub, H. Figiel, D. Chapelle, N. Kardjilov, A. Hilger, I. Manke, Int. J. Hydrog. Energy 36 (2011) 9751–9757.

[20] J.W. Hanneken, D.R. Franceschetti, R.B. Loftin, Z. Phys. Chem. 147 (1986) 47–59.

[21] M.R. Hawkesworth, J.P.G. Farr, J. Electroanal. Chem. Interfacial Electrochem. 119 (1981) 49–59.

[22] D.L. Jacobson, D.S. Hussey, E. Baltic, T.J. Udovic, J.J. Rush, R.C. Bowman JR., Int. J. Hydrog. Energy 35 (2010) 12837–12845.

[23] H. Sakaguchi, Y. Satake, K. Hatakeyama, S. Fujine, K. Yoneda, M. Matsubayashi, T. Esaka, J. Alloy Compd. 354 (2003) 208–215.

[24] G. Steyrer, J. Peisl, J. Less Common Met. 130 (1987) 147–153.

[25] B. Tsuchiya, M. Teshigawara, S. Nagata, K. Konashi, R. Yasuda, Y. Nishino, T. Nakagawa, M. Yamawaki, Nucl. Instrum. Method Phys. Res. B 190 (2002) 699–703.

[26] P.K. Pranzas, U. Bösenberg, F. Karimi, M. Münning, O. Metz, C.B. Minella, H.-W. Schmitz, F. Beckmann, U. Vainio, D. Zajac, E. Welter, T.R. Jensen, Y. Cerenius, R. Bormann, T. Klassen, M. Dornheim, A. Schreyer, Adv. Eng. Mater. 13 (2011) 730–736.

[27] C. Pohlmann, K. Herbrig, Ł. Gondek, N. Kardjilov, A. Hilger, H. Figiel, J. Banhart, B. Kieback, I. Manke, L. Röntzsch, J. Power Sources 277 (2015) 360–369.

[28] N. Kardjilov, A. Hilger, I. Manke, M. Strobl, M. Dawson, J. Banhart, Neutron News 20 (2009) 20–23.

[29] N. Kardjilov, A. Hilger, I. Manke, M. Strobl, M. Dawson, S. Williams, J. Banhart, Nucl. Instrum. Method Phys. Res. A 651 (2011) 47–52.

[30] N. Kardjilov, M. Dawson, A. Hilger, I. Manke, M. Strobl, D. Penumadu, F.H. Kim, F. Garcia-Moreno, J. Banhart, Nucl. Instrum. Method Phys. Res. A 651 (2011) 95–99.

[31] S.H. Williams, A. Hilger, N. Kardjilov, I. Manke, M. Strobl, P.A. Douissard, T. Martin, H. Riesemeier, J. Banhart, J. Instrum. 7 (2012) P02014.

[32] inCT, Octopus 8.6 manual, 2012.

[33] A. Gilbert, M. Deinert, Nucl. Instrum. Method Phys. Res. B 301 (2013) 23–28.

[34] H.M. Jaeger, S.R. Nagel, Sci. 255 (1992) 1523–1531.

[35] M. Ron, J. Alloy Compd. 283 (1999) 178–191.

[36] N. Takeichi, H. Senoh, T. Yokota, H. Tsuruta, K. Hamada, H.T. Takeshita, H. Tanaka, T. Kiyobayashi, T. Takano, N. Kuriyama, Int. J. Hydrog. Energy 28 (2003) 1121–1129.

[37] M. Okumura, A. Ikado, Y. Saito, H. Aoki, T. Miura, Y. Kawakami, Int. J. Hydrog. Energy 37 (2012) 10715–10723.

[38] F. Qin, L.H. Guo, J.P. Chen, Z. Chen, Int. J. Hydrog. Energy 33 (2008) 709–717.

[39] International Organization for Standardization, Transportable gas storage devices - Hydrogen absorbed in reversible metal hydride, ISO 16111, first ed., 2008.

[40] K. Herbrig, L. Röntzsch, C. Pohlmann, T. Weißgärber, B. Kieback, Int. J. Hydrog. Energy 38 (2013) 7026–7036.

[41] R.H. Wiswall, J.J. Reilly, Inorg. Chem. 11 (1972) 1691–1696.

Figure1

Click here to download Figure(s): Fig 1.eps

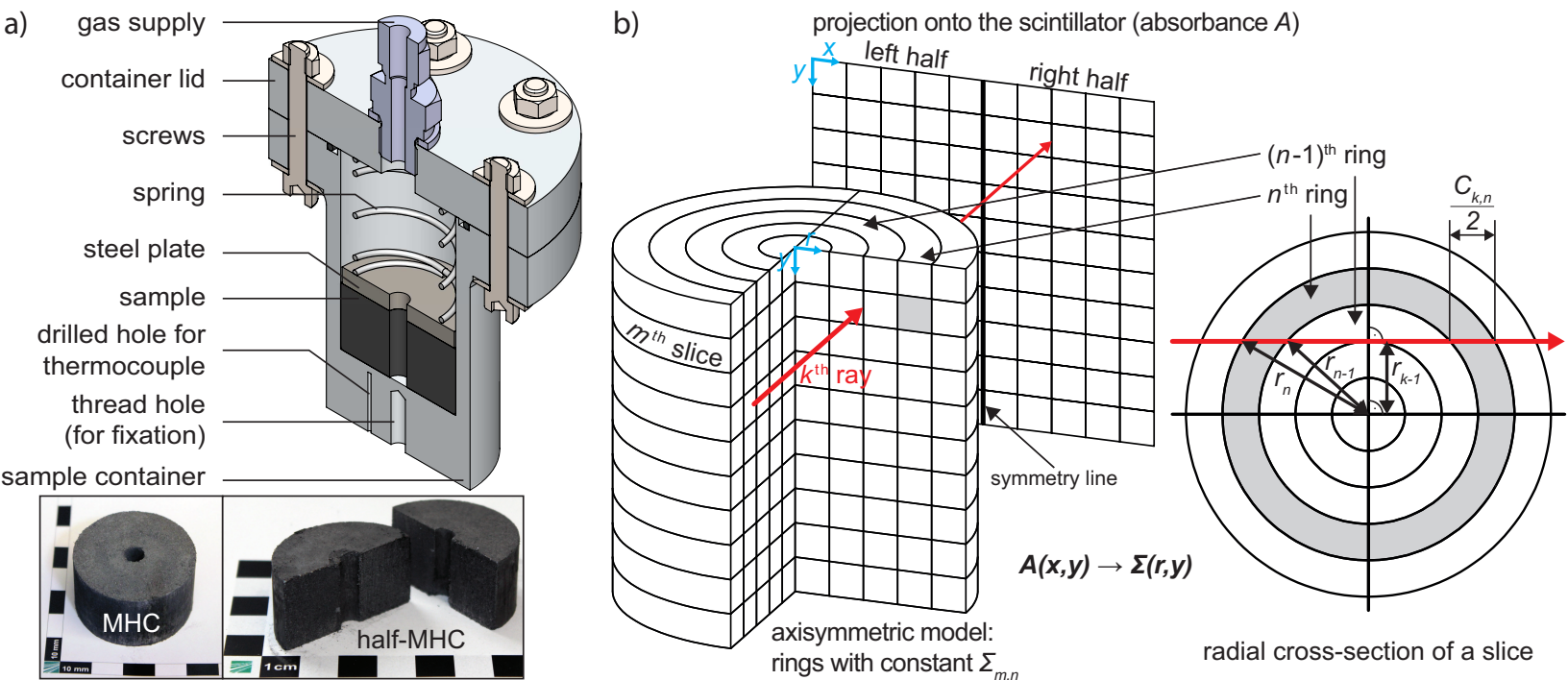

Figure2

Click here to download Figure(s): Fig 2.eps

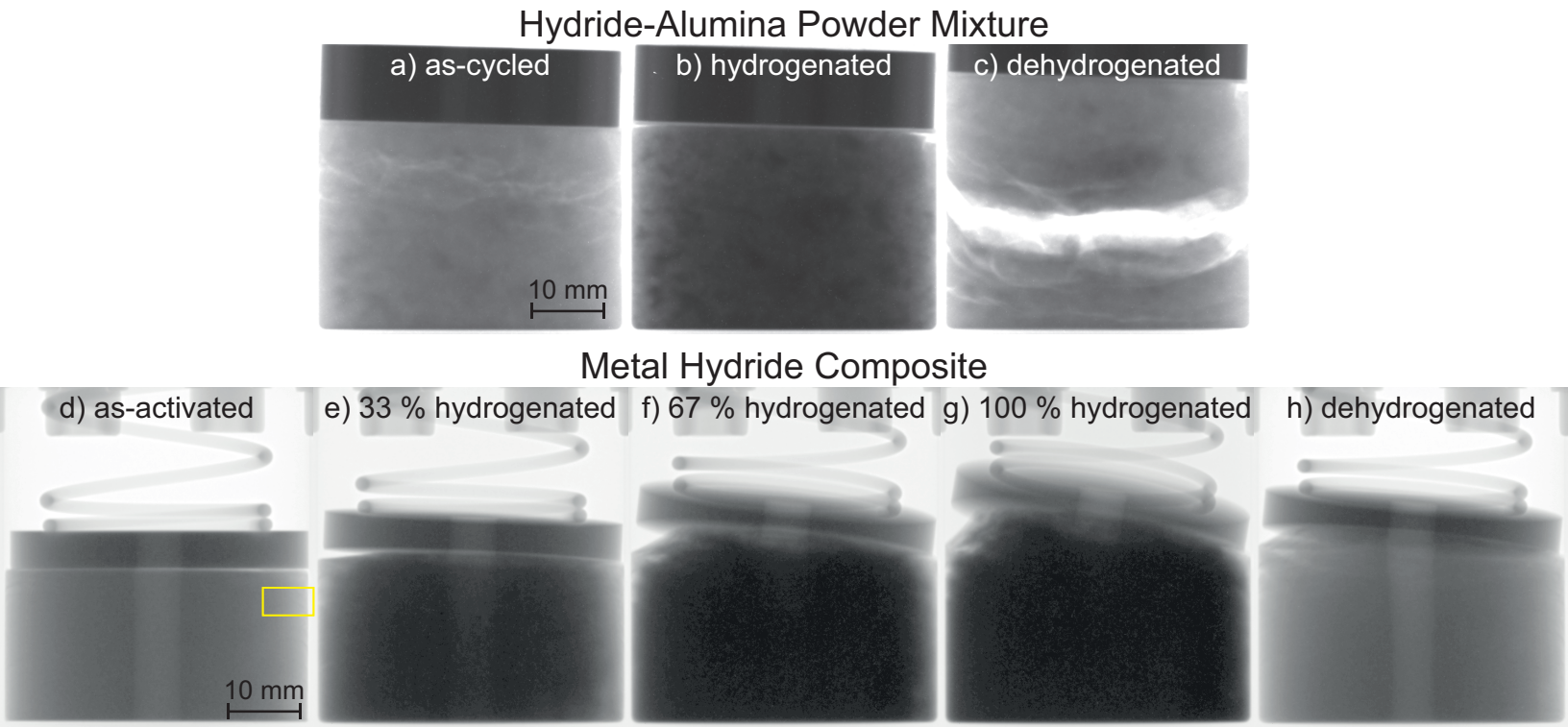

Figure3
Click here to download Figure(s): Fig 3.eps

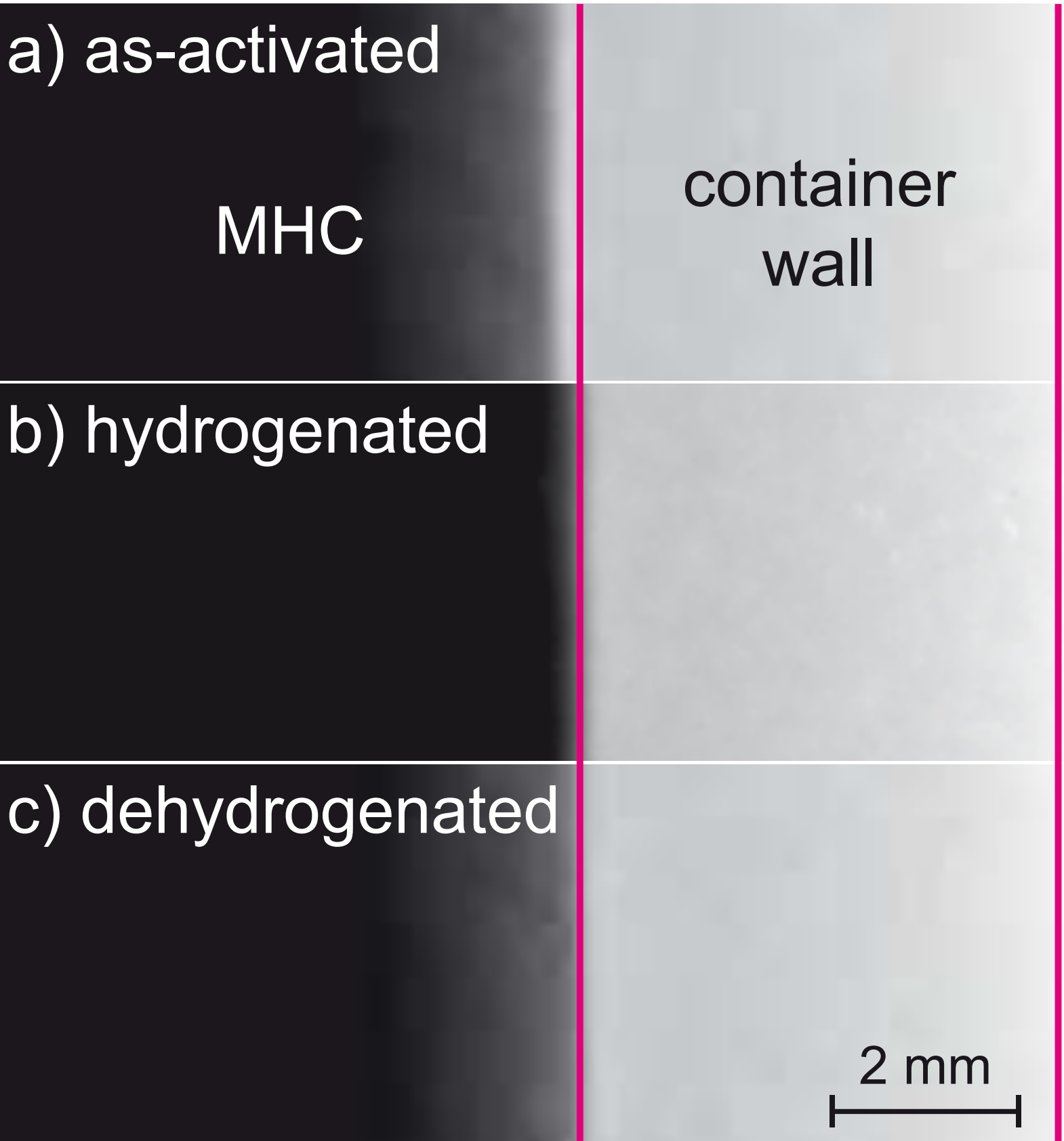

Figure4

Click here to download Figure(s): Fig 4.eps

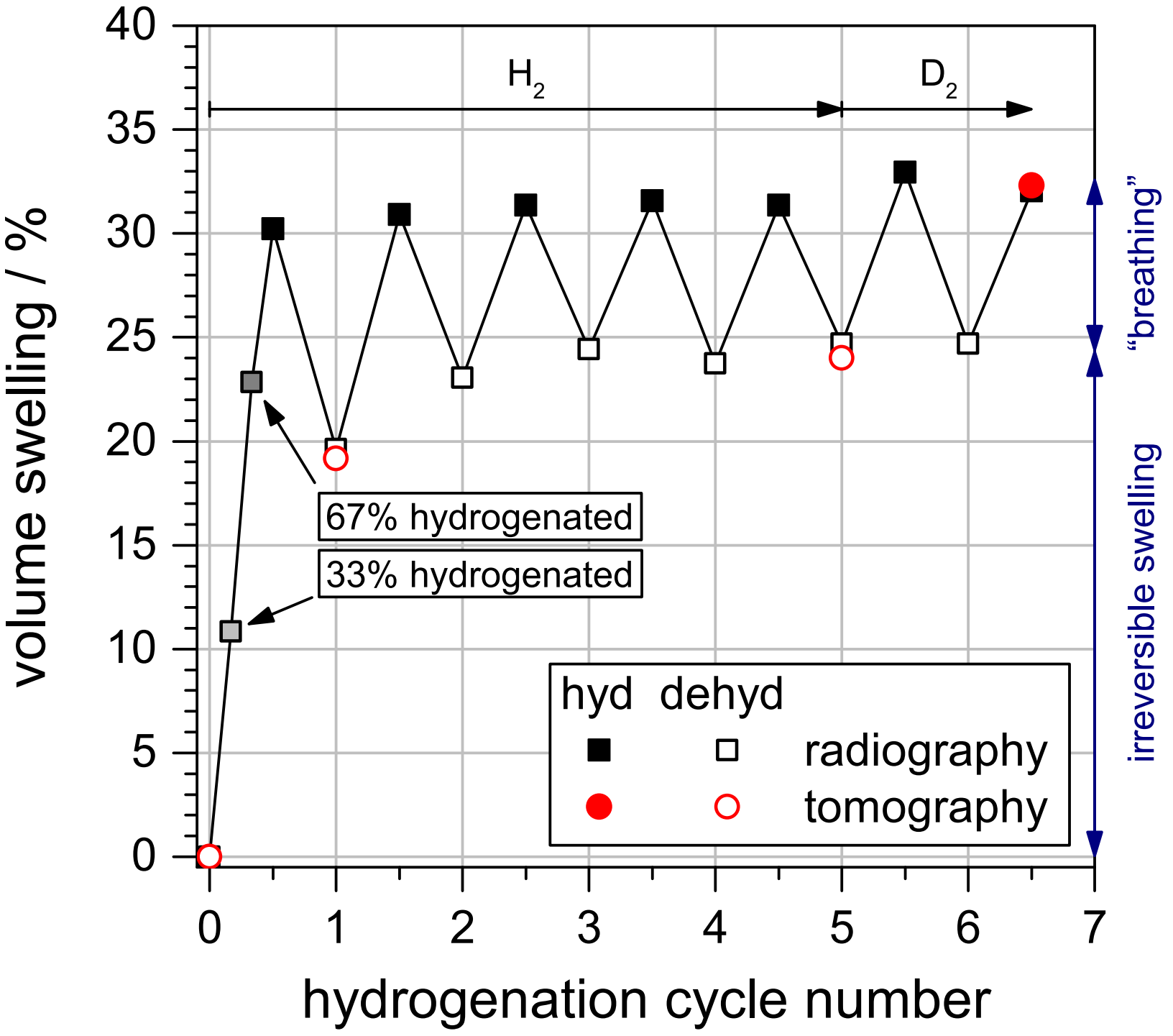

Figure5

Click here to download Figure(s): Fig 5.eps

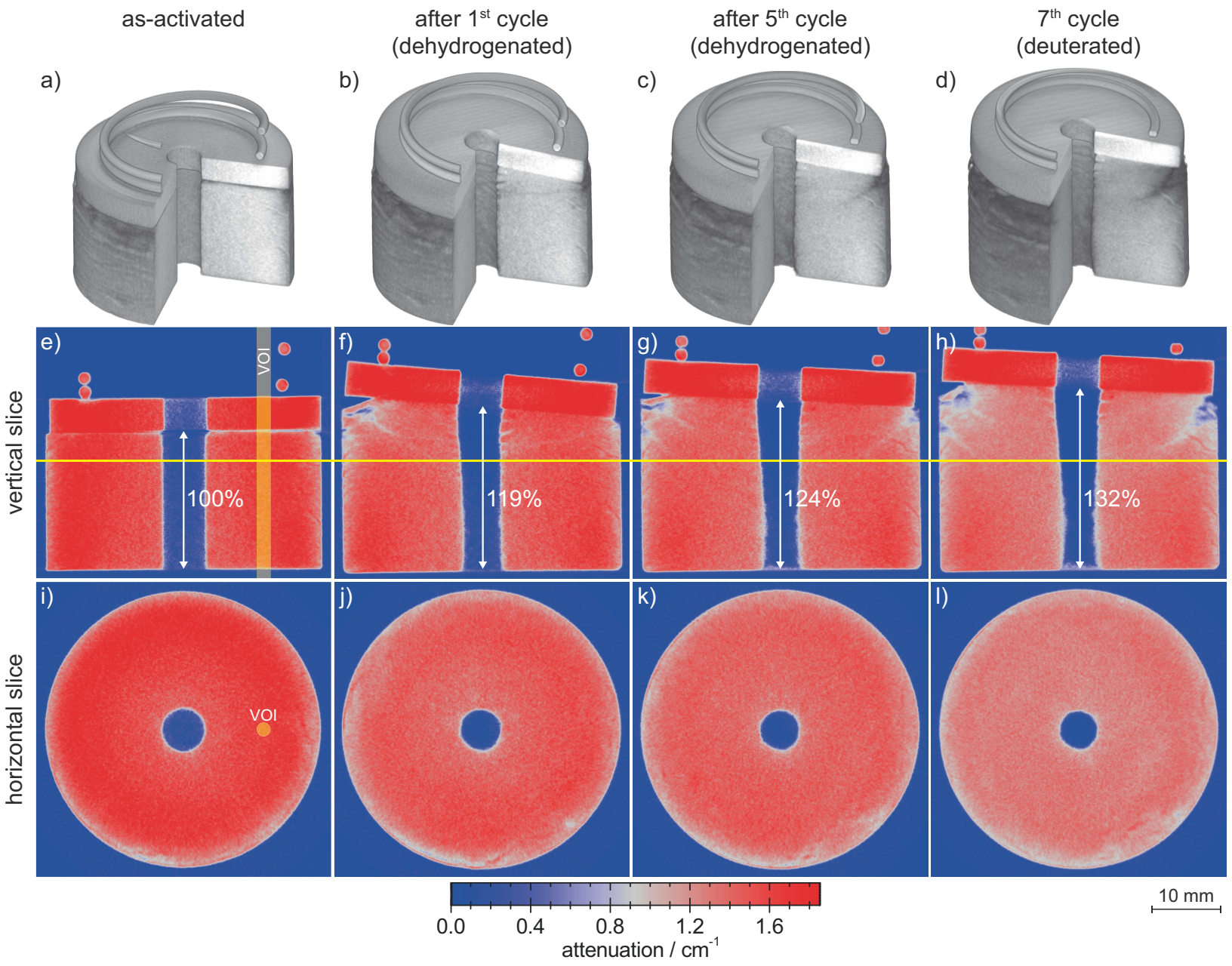

Figure6
Click here to download Figure(s): Fig 6.eps

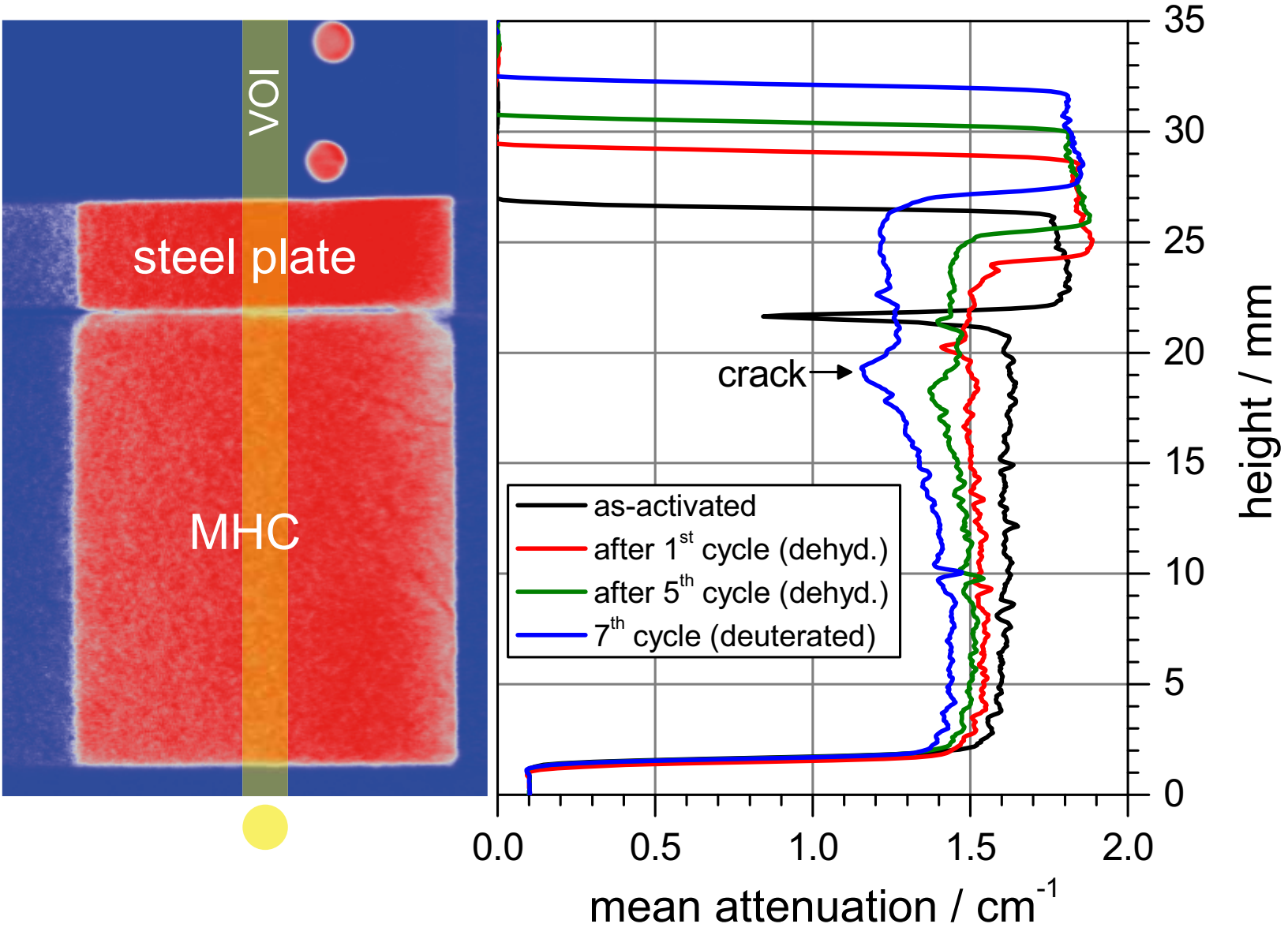

Figure7

Click here to download Figure(s): Fig 7.eps

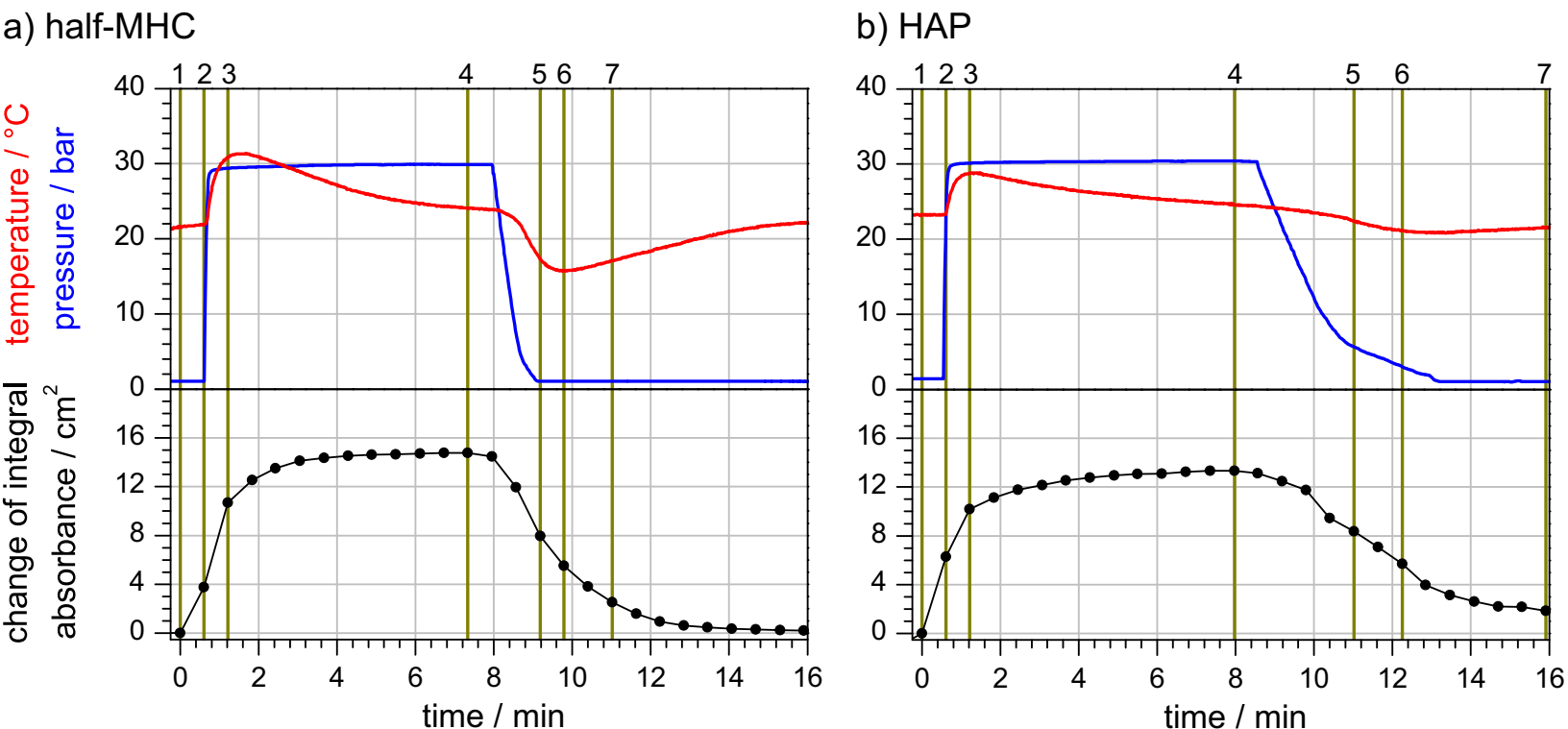

Figure8

Click here to download Figure(s): Fig 8.eps

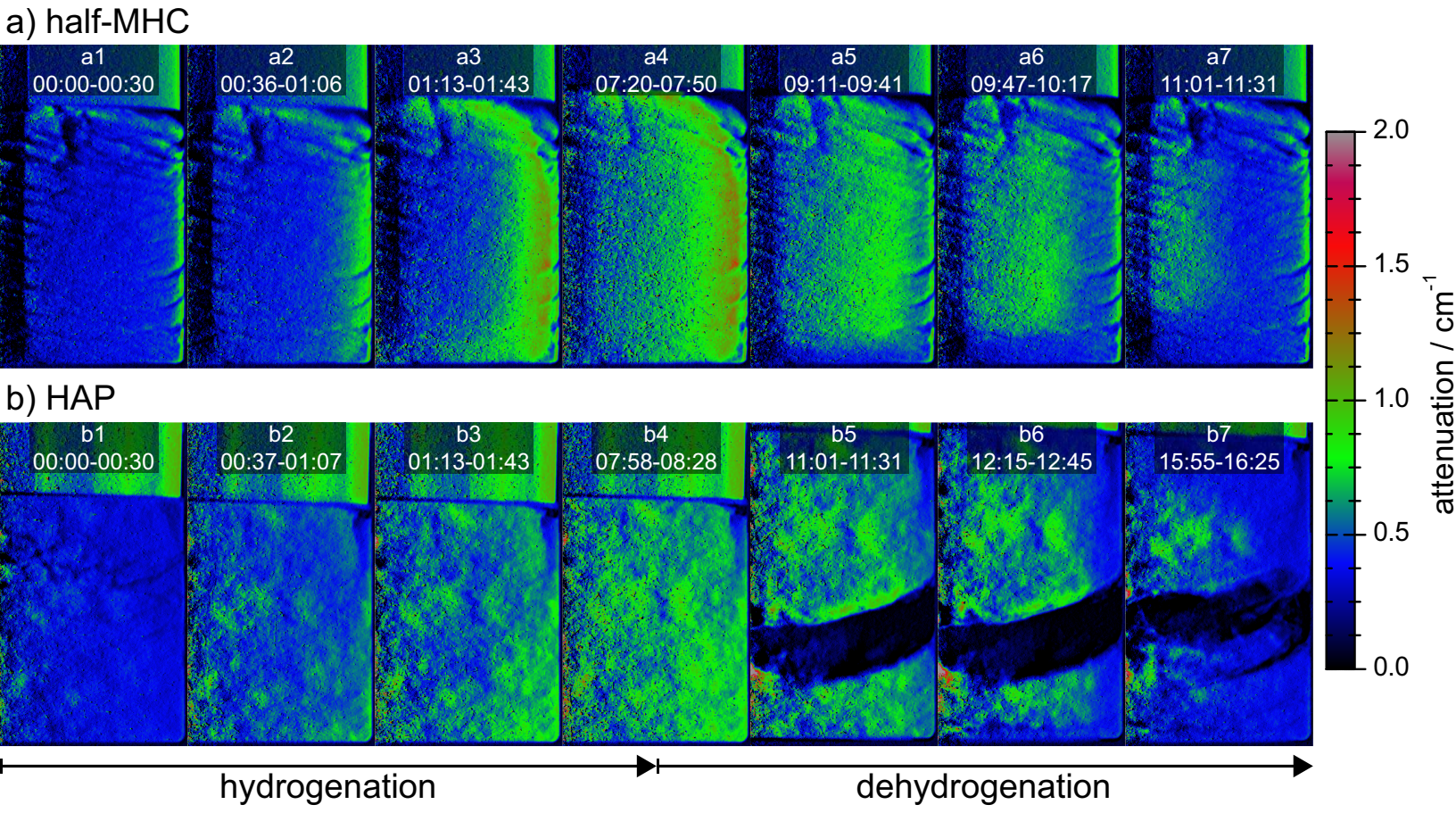

Figure Captions

Figure 1: (a) Schematic drawing of the experimental set-up used for in-situ neutron imaging of metal hydride composite (MHC) samples. (b) Ring model for the reconstruction of the spatial distribution of the attenuation coefficient based on a single projection of an axisymmetric sample (according to [33]). Here: $M = 10$, $N = 5$, $K = 5$, $k = 3$, n = 4, m = 2 (cf. equation (3) and (4)).

Figure 2: (a-c): In-situ neutron images after fast hydrogenation and fast dehydrogenation starting from the as-cycled state of a mixed hydride-alumina powder (HAP) sample (cf. video 1, online video data). (d-h): In-situ neutron images during slow (100 ml-H_2/min STP) hydrogenation and fast dehydrogenation (1st cycle) starting from the as-activated state (cf. video 2, online video data). The framed region in (d) is magnified in Figure 3.

Figure 3: Magnification of the framed region in Figure 2 d. The colored, vertical lines show the inner and outer container wall boundaries. Starting from the as-activated state (partial picture a, cf. Figure 2 d) the metal hydride composite (MHC) is hydrogenated (partial picture b, cf. Figure 2 g) and dehydrogenated (partial picture c, cf. Figure 2 h).

Figure 4: Volume swelling of the metal hydride composite (MHC) with respect to its initial volume throughout cyclic hydrogenation.

Figure 5: Volume rendered images (a-d), vertical (e-h) and horizontal (i-l) slices from the tomographic reconstruction of the metal hydride composite at different states during cyclic hydrogenation. The solid yellow line within the vertical slices indicates the plane of the corresponding horizontal slice below. The volume of interest (VOI in e) is specified by the half-transparent area used for density inhomogeneity analysis as depicted in Figure 6.

Figure 6: Mean attenuation of the metal hydride composite (MHC) within the selected area (volume of interest (VOI) on the left side, cf. Figure 5 e over height of the MHC.

Figure 7: Temperature, hydrogen gas pressure and change of the integral absorbance (refers to hydrogen content) during hydrogenation and dehydrogenation of (a) the halved metal hydride composite (half-MHC) and (b) the hydride-alumina powder mixture (HAP). The timestamps refer to the images shown in Figure 8 (cf. video 3, online video data).

Figure 8: Local radial attenuation coefficient reconstructed from single radiographs during hydrogenation and dehydrogenation of (a) the halved metal hydride composite (half-MHC) and (b) the hydride-alumina powder mixture (HAP). The corresponding temperatures, gas pressures, the integrals of the absorbance (hydrogen content) and timestamps of the images are shown in Figure 7 (cf. video 3, online video data).

Video Still1

Click here to download high resolution image

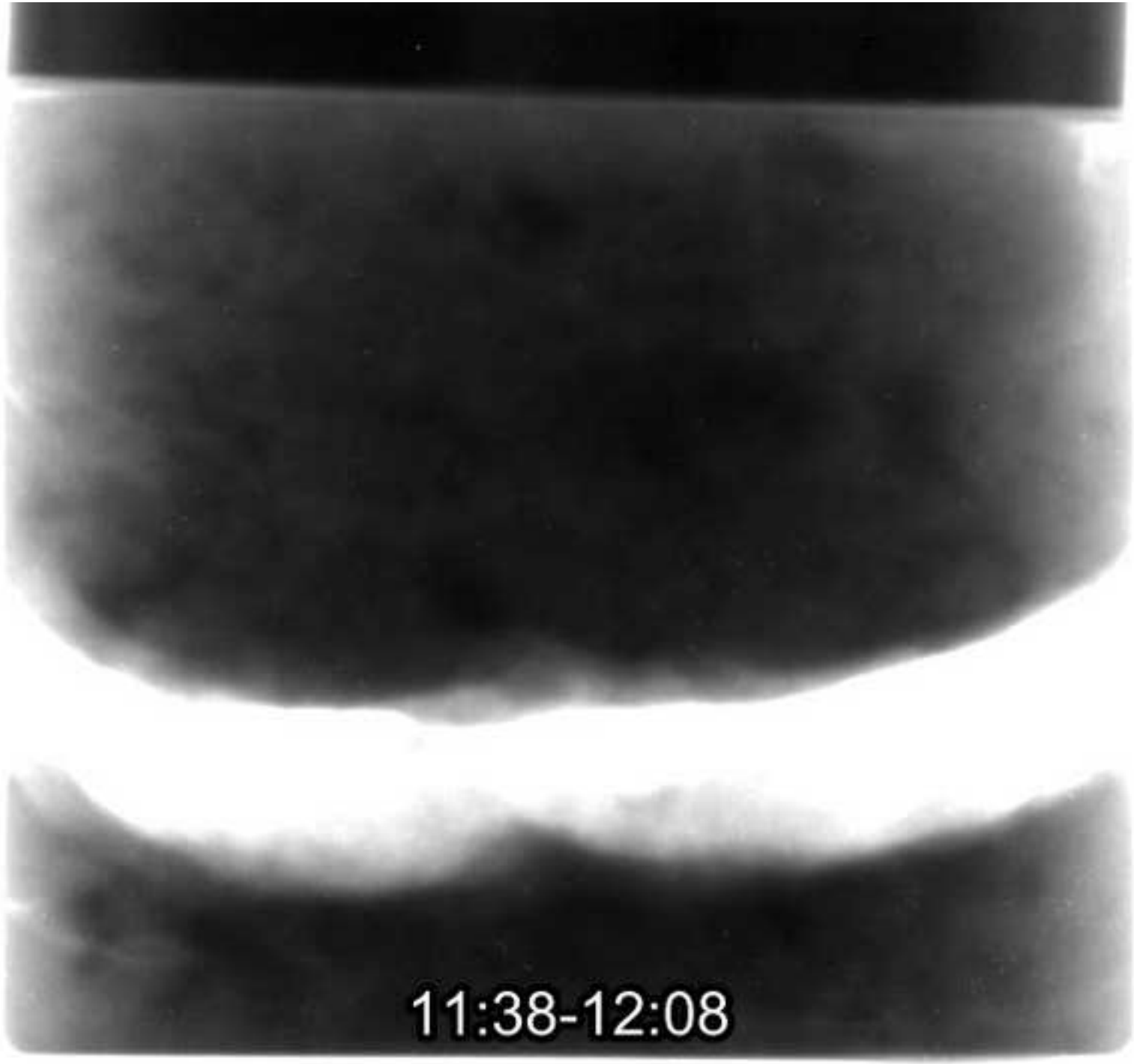

Video Still2

Click here to download high resolution image

Video Still3

Click here to download high resolution image